Electron–Nuclear Double Resonance Spectroscopy of ^{15}N-Enriched Phthalate Dioxygenase from *Pseudomonas cepacia* Proves That Two Histidines Are Coordinated to the [2Fe-2S] Rieske-Type Clusters†

Ryszard J. Gurbiel,‡,§ Christopher J. Batie,‖ Mohanram Sivaraja,‡ Anne E. True,‡ James A. Fee,*,⊥ Brian M. Hoffman,*,‡ and David P. Ballou*,‖

Department of Chemistry, Northwestern University, Evanston, Illinois 60208, Institute of Molecular Biology, Jagiellonian University, Krakow, Poland, Department of Biological Chemistry, The University of Michigan, Ann Arbor, Michigan 48109, and Isotope and Nuclear Chemistry Group, C-345, Los Alamos National Laboratories, Los Alamos, New Mexico 87545

Received October 27, 1988; Revised Manuscript Received February 8, 1989

ABSTRACT: We have performed ENDOR spectroscopy at microwave frequencies of 9 and 35 GHz at 2 K on the reduced Rieske-type [2Fe-2S] cluster of phthalate dioxygenase (PDO) from *Pseudomonas cepacia*. Four samples have been examined: (1) ^{14}N (natural abundance); (2) uniformly ^{15}N labeled; (3) [^{15}N]histidine in a ^{14}N background; (4) [^{14}N]histidine in a ^{15}N background. These studies establish unambiguously that two of the ligands to the Rieske [2Fe-2S] center are nitrogens from histidine residues. This contrasts with classical ferredoxin-type [2Fe-2S] centers in which all ligation is by sulfur of cysteine residues. Analysis of the polycrystalline ENDOR patterns has permitted us to determine for each nitrogen ligand the principal values of the hyperfine tensor and its orientation with respect to the g tensor, as well as the ^{14}N quadrupole coupling tensor. The combination of these results with earlier Mössbauer and resonance Raman studies supports a model for the reduced cluster with both histidyl ligands bound to the ferrous ion of the spin-coupled [Fe^{2+} ($S = 2$), Fe^{3+} ($S = {}^5/_2$)] pair. The analyses of ^{15}N hyperfine and ^{14}N quadrupole coupling tensors indicate that the geometry of ligation at Fe^{2+} is approximately tetrahedral, with the $(Fe)_2(N)_2$ plane corresponding to the g_1–g_3 plane, and that the planes of the histidyl imidazoles lie near that plane, although they could not both lie in the plane. The bonding parameters of the coordinated nitrogens are fully consistent with those of an sp^n hybrid on a histidyl nitrogen coordinated to Fe. Differences in ^{14}N ENDOR line width provide evidence for different mobilities of the two imidazoles when the protein is in fluid solution. We conclude that the structure deduced here for the PDO cluster is generally applicable to the full class of Rieske-type centers.

Iron–sulfur clusters of the Rieske type are associated with proteins of energy transduction and with a class of bacterial enzymes, typified by phthalate dioxygenase, which catalyze the oxidative degradation of aromatic carbon compounds. The Rieske iron–sulfur protein itself is associated with and essential to the function of energy-transducing, proteolipid complexes in the mitochondrial inner membrane (bc_1 or complex III), the thylakoid membrane of chloroplasts (b_6f), and the plasma membrane of certain bacteria; for review, see Rieske (1976), Malkin and Bearden (1978), Trumpower (1981a), Hauska et al. (1983), and Cramer et al. (1987). It appears that its function within these complexes is to participate in electron transfer from hydroquinones to the cytochrome *c* in a process coupled to proton translocation (Trumpower, 1981b; Palmer et al., 1985). The Rieske protein was first identified by J. S. Rieske and co-workers in 1964, who recorded its EPR and optical spectra and recognized them to be quite different from those of other iron–sulfur proteins (Rieske et al., 1964a,b). Subsequent studies during the next quarter of a century established the presence of a [2Fe-2S] cluster (Albracht & Subramanian, 1977) but failed to identify the structural differences distinguishing it from the ferredoxin-type [2Fe-2S] clusters that are coordinated to proteins by four cysteine ligands.

Characterization of the Rieske protein was impeded by its instability when isolated from the complex (Trumpower & Edwards, 1979). However, two recent developments have made it possible to characterize Rieske-type centers in some detail: isolation of a homogeneous and stable Rieske protein from *Thermus thermophilus* (Fee et al., 1984) and recognition that the bacterial dioxygenases contain Rieske-type centers (Twilfer et al., 1981; Fee et al., 1984; Geary et al., 1984; Batie et al., 1987). In these enzyme systems, the [2Fe-2S] center probably mediates electron transfer from another [2Fe-2S] protein to a mononuclear Fe^{2+} at the site of oxygenation, a role analogous to that in mitochrondria.

A battery of physical observations including visible, circular dichroism, EPR, ENDOR,[1] Mössbauer, and Raman spectroscopies indicates that the Rieske-type [2Fe-2S] cluster and its protein ligation are fundamentally the same in all cases. The distinguishing properties of the Rieske center are an EPR spectrum having $g_{av} \sim 1.91$ ($g_1 = 2.01$; $g_2 = 1.92$; $g_3 = 1.76$) compared with $g_{av} \sim 1.96$ for ferredoxins [cf. Bertrand et al. (1985)], a somewhat red-shifted visible absorption spectrum having a maximum absorptivity $\sim {}^2/_3$ that of ferredoxins, and

† This work was supported by the National Science Foundation, Grant DBM-8606575 (B.M.H.); by the National Institutes of Health, Grant HL 13531 (B.M.H.), GM 35342 (J.A.F.), and GM 20877 (D.P.B.); by the Stable Isotope Resource at Los Alamos (NIH Grant RR 02231); and by the Michigan Phoenix Memorial Project, No. 684.

‡ Northwestern University.
§ Jagiellonian University.
‖ The University of Michigan.
⊥ Los Alamos National Laboratories.

[1] Abbreviations: ENDOR, electron–nuclear double resonance; PDO, phthalate dioxygenase.

0006-2960/89/0428-4861$01.50/0

very different circular dichroic spectra (Bernhardt & Ruf, 1974; Degli Esposti et al., 1987). Moreover, the redox potentials of the Rieske-type proteins range from +350 to −150 mV while those of ferredoxins are much lower, near −400 mV; cf. Fee et al. (1986) for review.

Analysis of these physical and compositional studies led to the following conclusions about the structure of the cluster:

(1) The oxidized form contains two high-spin ferric ions that are antiferromagnetically spin coupled to give $S_{tot} = 0$.

(2) The reduced form contains one high-spin ferric ion spin coupled to one high-spin ferrous ion, giving a total spin $S = {}^1/_2$ as described by the model of Gibson et al. (1966).

(3) The amino acid composition of the *T. thermophilus* protein (Fee et al., 1984) indicates that only two cysteine residues can be coordinated to the [2Fe-2S] cluster.

(4) Comparison of the Mössbauer parameters of the Rieske centers in three different proteins with those of several [2Fe-2S] ferredoxins led Münck and co-workers (Fee et al., 1984) to suggest the two iron ions have four sulfur ligands (two cysteinate and two bridging sulfides) and two non-sulfur ligands and to consider the possibility that in the reduced centers both of the latter are coordinated to the Fe^{2+} ion. An analysis of the Rieske center's EPR g values by Bertrand et al. (1985) was consistent with the presence of ligands to the ferrous site that are more electronegative than sulfide. The same conclusion had been reached earlier by Blumberg and Peisach (1974), who analyzed the EPR parameters of many [2Fe-2S] containing proteins.

(5) ENDOR and electron spin-echo spectra of the *Thermus* Rieske protein and phthalate dioxygenase (PDO) of *Pseudomonas cepacia* (Cline et al., 1985) and ENDOR spectra of mitochondrial Rieske protein (Telser et al., 1987) demonstrated the presence of a nitrogen atom(s) coordinated to the cluster.

(6) Resonance Raman spectra of *Thermus* Rieske protein and PDO of *P. cepacia* (Kuila et al., 1987; Kuila et al., unpublished results) exhibit at least 12 Raman-active vibrational modes, leading to the conclusion that the structure of the complex has C_{2v} symmetry with at least two non-sulfur ligands coordinated to one Fe. By comparison, the ferredoxin center has no more than nine Raman-active modes and possesses D_{2h} symmetry. Earlier resonance Raman work had excluded tyrosine as one of the ligands (Fee et al., 1984).

These observations prompted the following hypothetical working model of the Rieske cluster's structure in which terminal S and N atoms are provided by cysteine and histidine imidazole:

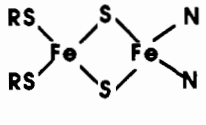

Certain aspects of this hypothesis can be tested through specific isotope labeling studies, and PDO from *P. cepacia* is an excellent candidate for this approach: it is a stable protein that contains a single [2Fe-2S] Rieske-type cluster, it can be expressed at high levels in induced cells (5–7% of soluble protein), and it is easily obtained in pure form (Batie et al., 1987). We report here 9- and 35-GHz ENDOR studies on globally and selectively ^{15}N-enriched PDO prepared from *P. cepacia*. The results show unequivocally that two imidazole nitrogens from histidine are coordinated to the cluster. Through analysis of the polycrystalline ENDOR spectra (Hoffman et al., 1984, 1985; True et al., 1988), we have established that there are two histidines coordinated to Fe^{2+}, described the coordination geometry about this ion, and determined the bonding parameters of the two nitrogen ligands.

Procedures and Theory

Sample Preparation. We prepared four different samples of PDO from *P. cepacia*, each with a specific isotopic labeling pattern: (sample 1) ^{14}N (natural abundance); (sample 2) uniformly ^{15}N labeled (≥99%); (sample 3) [^{15}N]histidine (≥95%) in ^{14}N background; (sample 4) [^{14}N]histidine in ^{15}N background (≥99%). Isotopically enriched histidine was obtained from the NIH-supported Stable Isotope Resource at Los Alamos; $(^{15}NH_4)_2SO_4$ was purchased from MSD Isotopes.

Samples 1 and 2 were purified from strain DB01 of *P. cepacia*, as described previously (Batie et al., 1987). The growth medium used in the preparation of sample 2 differed from our standard medium (Bull & Ballou, 1981) in that it contained $(^{15}NH_4)_2SO_4$ (99 atom % ^{15}N) instead of $(NH_4)_2HPO_4$ (natural abundance) as a nitrogen source. Samples 3 and 4 were purified from strain DB0110, a mutant of *P. cepacia* DB01 that requires histidine for growth. This strain was the gift of Drs. G. Zylstra and R. H. Olsen of The University of Michigan; it was isolated following treatment of strain DB01 with *N*-methyl-*N'*-nitro-*N*-nitrosoguanidine (Zylstra, 1987).

Samples 3 and 4 were prepared from bacteria grown at 37 °C on a histidine-supplemented minimal medium (His–phthalate–mmo) that contained phthalate as the sole carbon source [formulation derived from Olsen and Shipley (1973)]. This medium differs from our standard medium (Bull & Ballou, 1981) in that it does not contain yeast extract. The His–phthalate–mmo medium contained the following components (preparation of which is described next): 1750 mL of distilled water, 80 mL of $NaKP_i$ buffer, 40 mL of Mineral A, 10 mL of Fe-EDTA, and 20 mL of D,L-histidine. Prior to the addition of histidine, media was sterilized by autoclaving; then, sterile histidine was added.

All stock solutions were made up in distilled water. $NaKP_i$ buffer, pH 6.8, was prepared by mixing 1 M KH_2PO_4 and 1 M Na_2HPO_4 in a ratio of 19:22. Mineral B contained in 1 L 3.18 g of Na_2EDTA, 1.10 mg of $ZnSO_4$, 1.54 g of $MnSO_4$, 0.39 g of $CuSO_4$, 0.25 g of $Co(NO_3)_3$, 1 mL of 17 mg/mL $Na_2B_4O_7$, and 4 drops of concentrated H_2SO_4. Mineral A contained in 1 L 10 g of Na_2EDTA, 14.45 g of $MgSO_4$, 3.34 g of $CaCl_2 \cdot 2H_2O$, 9.3 mg of $(NH_4)_6Mo_7O_{24} \cdot H_2O$, and 50 mL of mineral B. Fe-EDTA consisted of 7 g of $Fe(NH_4)_2(SO_4)_2$ and 10.0 g of Na_2EDTA in 1 L of distilled water. Ammonium sulfate solution consisted of 100 g of ammonium sulfate (either ^{14}N or ^{15}N) in 1 L; Dipotassium phthalate was made up to 0.5 M concentration. D,L-Histidine (either D,L-[1,3-$^{14}N_2$]- or D,L-[1,3-$^{15}N_2$]histidine obtained from the Los Alamos NIH Stable Isotope Resource) was made up at 50 mM. The histidine solution was sterilized by microfiltration; all other solutions were sterilized by autoclaving.

Preliminary trials indicated that 0.5 mM histidine was the minimum concentration sufficient to support rapid growth of DB0110 on phthalate-containing minimal media. An additional supplement of histidine (0.5 mmol/L) was added when $A_{540} > 1.3$. Thus 400 mg of histidine was used in growing 2 L of culture. The cells were harvested when $A_{540} > 2.5$. Samples 3 and 4 were purified as before (Batie et al., 1987), except that in the purification of sample 3 the last step (ion-exchange chromatography on DEAE-Sepharose) was omitted.

We used the method of Matthews[2] to determine the specificity with which histidine was labeled in PDO. DB0110 was

[2] Dr. Rowena G. Matthews, University of Michigan, personal communication.

grown on His–phthalate–mmo medium that included [^{14}C-(U)]histidine (1 μCi per 20 mL) purchased from ICI; the cells were harvested in mid-log phase. The cells were resuspended in 100 μL of 10 mM Tris-HCl, pH 7.4–5 mM $MgCl_2$ (buffer A) and disrupted by sonication. The homogenate was centrifuged for 10 min in a Beckman microfuge, and the supernatant solution was collected. RNase and DNase (2 μL of a solution containing 2 mg/mL each enzyme in buffer A) were added, and the mixture was incubated for 10 min at 0 °C. The protein fraction was precipitated by addition of trichloroacetic acid (TCA); 167 μL of 30% TCA and 663 μL of water were added to 100 μL of DNase–RNase-treated cell extract. After a 30-min incubation at 0 °C, the precipitated protein was collected by centrifugation. Amino acid analysis was performed on the pellet by the method of Tarr (1986), and the ^{14}C content of each amino acid fraction was determined by scintillation counting. The specific activity of the starting histidine was determined by analysis of a parallel sample of growth medium that was not inoculated with bacteria.

The validity of our experiments depends on the use of enzyme specifically labeled with [^{15}N]histidine. As this compound is precious, we first used [^{14}C]histidine to test the specificity of labeling by the method described above. We found that histidine retained high specific activity, indicating no serious dilution of the label. In addition, although some label was incorporated into several amino acids (Ile, Pro, Tyr, Arg, Glu, and Phe), the specific activity of ^{14}C in these other amino acids was only $^1/_5$ to $^1/_3$ that of histidine.

Protein samples (2–4 mM) were prepared in 100 mM HEPES buffer, pH 8, and placed in EPR/ENDOR tubes with a small excess of sodium dithionite. Active volumes were ca. 200 μL for X-band samples and ca. 20 μL for Q-band samples. All samples had been fully reconstituted with Fe^{2+} in the mononuclear site of PDO (Batie et al., 1987). EPR spectra were recorded at <2 K to verify that each tube contained the expected species.

ENDOR Measurements. ENDOR spectra were recorded on either a modified Varian Assoc. E109 spectrometer described previously (Venters et al., 1986) or a modified Varian Assoc. 35-GHz spectrometer. The 35-GHz (Q-band) ENDOR spectrometer consists of a Varian Assoc. E-110 microwave bridge interfaced to a E109 EPR console. The radio-frequency instrumentation and 100-kHz field-modulation detection are as previously described for the 9.5-GHz (X-band) ENDOR spectrometer (Venters et al., 1986). Experiments were performed with a silvered TE_{011} sample cavity held at ~2 K in a Janis Corp. liquid helium immersion Dewar; mutually perpendicular field-modulation and radio-frequency coils run through the cavity.

The first-order ^{14}N ENDOR spectrum for a single orientation of a paramagnetic center consists, in principle, of four transitions at frequencies given by eq 1 (Abragam & Bleaney,

$$\nu_{\pm,m}(^{14}\mathrm{N}) = \frac{A(^{14}\mathrm{N})}{2} \pm \nu(^{14}\mathrm{N}) + \frac{3P(^{14}\mathrm{N})}{2}(2m - 1) \qquad (1)$$

1970; Atherton, 1973), where A and P are the angle-dependent ^{14}N hyperfine and quadrupole coupling constants, respectively, the nuclear spin projection is $m = 1$ or 0, and $\nu(^{14}\mathrm{N})$ is the nuclear Larmor frequency; $\nu(^{14}\mathrm{N}) = g(^{14}\mathrm{N})\beta_N H_0$ (Abragam & Bleaney, 1970). When, as is true here, $A(^{14}\mathrm{N})/2 > \nu(^{14}\mathrm{N}) > P(^{14}\mathrm{N})$, eq 1 describes a four-line pattern centered at $A(^{14}\mathrm{N})/2$, consisting of a Larmor-split doublet further split by the quadrupolar term.

In some biological centers, the ^{14}N quadrupole splitting is well resolved, and a given type of ^{14}N shows the expected four-line pattern; but in many others it is not, and only a single Larmor-split doublet centered at $A(^{14}\mathrm{N})/2$ is observed. This variability causes problems in assigning ^{14}N resonances from a center of unknown composition. A four-line pattern that can be described by eq 1 might indeed arise from a single type of nitrogen with resolved quadrupole couplings. However, it might also represent the signals from two inequivalent ^{14}N, neither of which exhibits resolved quadrupole splittings.

This ambiguity can be resolved through ^{15}N isotopic enrichment. A ^{15}N nucleus has $I = {}^1/_2$ and does not exhibit a quadrupole splitting. A single-crystal ^{15}N ENDOR spectrum consists of a Larmor-split doublet with only two lines; their approximate frequencies are

$$\nu_{\pm}(^{15}\mathrm{N}) = \frac{A(^{15}\mathrm{N})}{2} \pm \nu(^{15}\mathrm{N}) \qquad (2)$$

where $\nu(^{15}\mathrm{N}) = g(^{15}\mathrm{N})\beta_N H_0$. Thus, a four-line ^{15}N ENDOR pattern would necessarily imply the presence of two inequivalent nitrogen sites. Moreover, the resonance frequencies of ^{14}N and ^{15}N are related by fundamental nuclear properties

$$\frac{A(^{15}\mathrm{N})}{A(^{14}\mathrm{N})} = \frac{\nu(^{15}\mathrm{N})}{\nu(^{14}\mathrm{N})} = \frac{g(^{15}\mathrm{N})}{g(^{14}\mathrm{N})} = -1.403 \qquad (3)$$

and thus assignment of an ENDOR spectrum for one isotopic species directly predicts features of the other (eq 1 and 2). For example, the ENDOR pattern of a ^{15}N nucleus would be a doublet centered at a frequency 1.4 times greater than that for the corresponding ^{14}N, and the doublet splitting, $2\nu(^{15}\mathrm{N})$, also would be 1.4-fold greater.

Interference from stronger, overlapping ^{1}H ENDOR signals is a common complication in interpreting nitrogen ENDOR patterns taken at X-band microwave frequencies [e.g., Roberts et al. (1984)]. However, the nitrogen ENDOR patterns are centered at a frequency determined by the hyperfine coupling constant, a molecular parameter, whereas a set of magnetically equivalent protons gives a pair of ENDOR transitions ($\nu_\pm$) centered about the free-proton Larmor frequency

$$\nu_\pm = \nu_H \pm A^H/2 \qquad (4)$$

$\nu_H = (g_H\beta_n/\beta_e)[\nu(\mathrm{M})/g_{obs}]$, which varies with the EPR spectrometer frequency. For a fixed g_{obs} the center of the proton resonance pattern shifts in proportion to the microwave frequency, $\nu(\mathrm{M})$. An increase of $\nu(\mathrm{M})$ from 9 GHz (X-band) to 35 GHz (Q-band) increases ν_H (at $g \sim 2$) from ~14 to ~53 MHz, which eliminates spectral overlap of proton signals with those of ^{14}N (or other nuclei).

The samples employed in this study are frozen solutions and thus contain a random distribution of all protein orientations. However, ENDOR spectra taken with the magnetic field set at the extreme edges of the EPR spectrum, near the maximal or minimal g values, give single-crystal-like patterns from the subset of molecules for which the magnetic field happens to be directed along a g tensor axis (Rist & Hyde, 1970). Although an ENDOR spectrum obtained with an intermediate g value does *not* arise from a single orientation, it does represent a well-defined subset of molecular orientations (Hoffman et al., 1984, 1985). As described in detail recently (True et al., 1988), the principal values of a hyperfine tensor and its orientation relative to the g tensor axis frame can be determined by simulating a set of ENDOR spectra recorded at g values (fields) across the EPR envelope. These simulations and those reported here do not use the approximate eq 1, 2, and 4 but rather a more exact treatment (Thuomas & Lund, 1974). In simulating ^{14}N ENDOR spectra it was sufficient to consider only the first-order quadrupole interaction because the second-order quadrupole contributions (Iwaskai, 1974) are

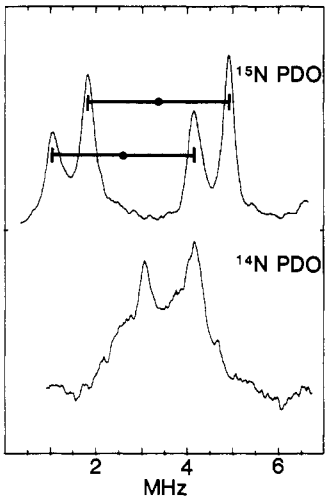

FIGURE 1: ENDOR spectra of (top) ^{15}N-enriched (sample 2) and (bottom) ^{14}N natural abundance (sample 1) PDO from *P. cepacia* taken at $g_2 = 1.92$. The assignment to $A/2$ (●) and twice the Larmor frequency (|−|) of each doublet are indicated on the spectra. Conditions: H_0 = 3596 (^{14}N) and 3588 G (^{15}N); T = 2 K; microwave power, 10 μW; 100-kHz field modulation, 1 G; rf power, 20 W; rf scan rate, 2.5 MHz/s; 1000 scans.

found to be negligibly small. For example, at g_1 the second-order quadrupole correction to $\nu_{+,1}(^{14}N)$ is 0.014 MHz.

The A tensor for each interactive nucleus can be taken as diagonal within its own principal axis coordinate frame, in which case it can be described by the three diagonal components and the three Euler angles (α, β, γ) (Mathews & Walker, 1965; True et al., 1988) that specify the orientation of the nuclear frame (**A**) with respect to the reference, **g** frame. If we begin with **A** and **g** coaxial, α refers to rotation of the **A** tensor around its A_3 axis, β is a rotation about the new A_2 axis, and γ is the subsequent rotation around the new A_3 axis; these angles are illustrated in Figure 4.

Results and Discussion

Identification and Assignment of Two Nitrogenous Ligands Coordinated to the [2Fe-2S] Cluster. The frozen-solution EPR spectrum of PDO is characteristic of a g tensor with rhombic symmetry; the g_i were given in the introduction. ENDOR measurements were performed at X-band [ν(M) ~ 9.4 GHz] across the EPR spectrum of PDO from *P. cepacia* grown either on natural abundance (^{14}N) or ^{15}N-enriched media. As previously reported (Cline et al., 1985), the ENDOR spectrum at g_2 of natural abundance PDO (sample 1) shows a broad pattern of ^{14}N resonances centered at ~3.5 MHz (Figure 1). No attempts at detailed analysis of this signal were made in the original report; this will be done below. Spectra of ^{15}N-enriched PDO (sample 2, Figure 1) taken at g_2 exhibit two sharp doublets that are centered at 2.55 and 3.35 MHz; they can be assigned to ^{15}N because each shows a splitting of $2\nu(^{15}N)$ = 3.1 MHz. An ENDOR pattern at g_2 corresponds to a distribution of orientations, and hyperfine anisotropy might, in principle, cause a single ^{15}N to give more than a single pair of peaks. However, an ENDOR spectrum (see below) taken at g_1 corresponds to a unique molecular orientation and also exhibits two doublets; this proves that the ^{15}N ENDOR signals represent two magnetically distinct nitrogenous ligands coordinated to the [2Fe-2S] cluster.

These two nitrogenous ligands are identified as histidines from the results of ENDOR measurements on PDO that was specifically labeled with [^{15}N]histidine. Figure 2A is a Q-band ENDOR spectrum of sample 3 taken at g_2. It shows the nitrogen resonances of [^{15}N]histidine-labeled PDO obtained

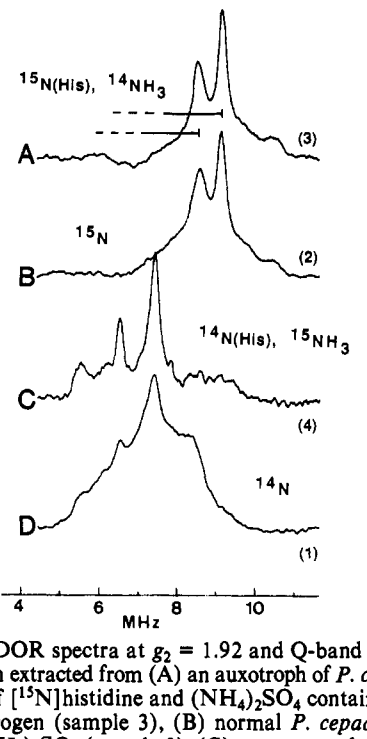

FIGURE 2: ENDOR spectra at g_2 = 1.92 and Q-band frequency of the PDO protein extracted from (A) an auxotroph of *P. cepacia* grown on a medium of [^{15}N]histidine and $(NH_4)_2SO_4$ containing natural-abundance nitrogen (sample 3), (B) normal *P. cepacia* grown on ^{15}N-labeled $(NH_4)_2SO_4$ (sample 2), (C) an auxotroph of *P. cepacia* grown on a medium of histidine containing natural-abundance nitrogen and ^{15}N-labeled $(NH_4)_2SO_4$ (sample 4), and (D) normal *P. cepacia* grown on $(NH_4)_2SO_4$ containing natural-abundance nitrogen (sample 1). For ease of reference, the traces are labeled with the sample number in parentheses. Conditions: T = 2 K; microwave power, 50 μW; microwave frequency, 35.3 GHz; 100-kHz field modulation, 3.2 G; rf power, 20 W; scan rate, 2.5 MHz/s; 300 scans.

from strain DB0110. The resonances at ν_+ = 8.2 and 9.2 MHz observed at Q-band correspond through eq 2 to the ν_+ = 4.1 and 4.8 MHz lines observed at X-band (Figure 1). Curve B shows the same spectral region for uniformly ^{15}N-labeled PDO (sample 2, Procedures and Theory). The spectra are identical, demonstrating that the two nitrogen-containing ligands are histidines.[3]

Comparison of curve C (sample 4) and curve D (sample 1) provides additional proof that both nitrogenous ligands are histidine residues. Curve C is the spectrum of PDO labeled with $(^{15}NH_4)_2SO_4$ and [^{14}N]histidine (sample 4, Procedures and Theory); curve D is the spectrum of [^{14}N]PDO (natural isotopic abundance; sample 1, Procedures and Theory). Sharp features from ^{14}N at 7.4, 6.5, and 5.6 MHz are visible both in curve D, the spectrum of [^{14}N]PDO, and in curve C, that from PDO with [^{14}N]His in a ^{15}N background. The absence of additional ^{15}N signals in curve C, where non-histidyl nitrogens have been labeled with ^{15}N, indicates that the only nitrogen ligands to the [2Fe-2S] center are from histidine.

The ^{14}N resonances of sample 4 (curve C) are more resolved than those of sample 1 (curve D); this appears to result from unidentified relaxation processes associated with the bulk ^{14}N nuclei of the protein. An alternative interpretation might be that curve D is a summation of curve C and additional broad resonance centered at ~7–8 MHz. However, such a resonance could not be the result of weakly coupled, distant ^{14}N because it is absent in the spectrum of sample 3, and in any case it should be centered at ν_N = 4.4 MHz (eq 3). Furthermore, a broad resonance in curve D could not derive from a non-

[3] The only restriction on this conclusion is that there be no metabolic pathway that produces another potential nitrogenous ligand by metabolism of the added histidine, which is unlikely.

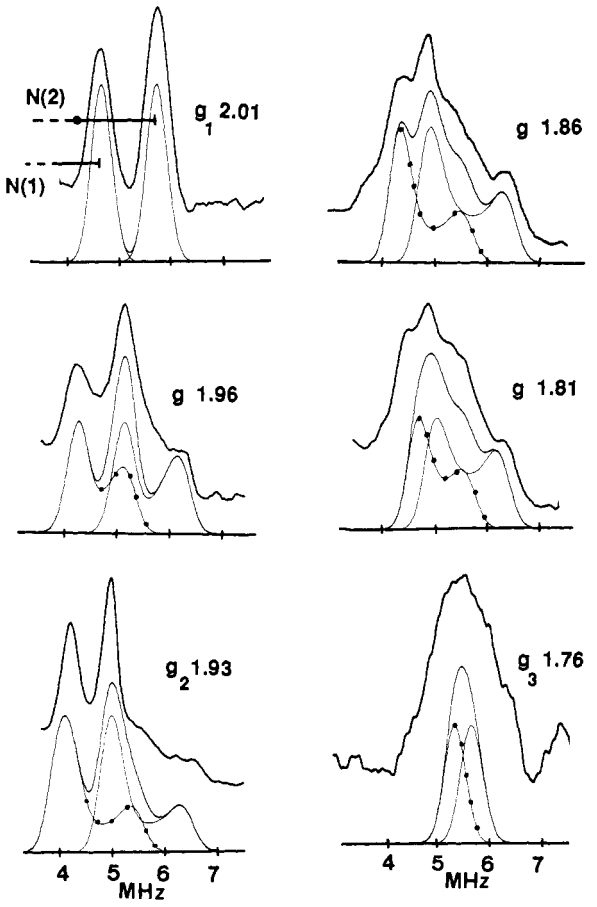

FIGURE 3: ^{15}N ENDOR spectra of the two ^{15}N sites of phthalate dioxgenase (sample 1) showing the ν_+ resonances at selected magnetic fields. Computer simulations for the individual ^{15}N and their sum employ the hyperfine interaction parameters of Table I and the algorithms given by True et al. (1988); they are shown below the corresponding spectra. The curves for N(1) are indicated by (●), as needed, and the bold lines are the sum of simulations for N(1) and N(2). The component line widths were taken to be equal for the two sites (0.2 MHz) and independent of angle; relative intensities for the individual sites are normalized. Differential broadening of the simulated ENDOR peaks was seen upon inclusion of an EPR line width of more than 20 G; all spectra were simulated with EPR line widths of 20 G. Experimental conditions are as described in Figure 1, with a microwave frequency of 9.6 GHz and g values as indicated. Each spectrum is the average of 1000 scans.

histidyl nitrogenous ligand because in uniformly ^{15}N-labeled PDO such a ligand would give a ^{15}N pattern that is centered at ~10–11 MHz and extends to ~14–15 MHz; this is not seen (sample 2, curve B). We show immediately below that all features of ^{15}N spectra of samples 2 and 3 can be accounted for in terms of two N's derived from histidines and that there are therefore no other nitrogens magnetically coupled to the center.

Determination of ^{15}N Hyperfine Tensors. Determination of the ^{15}N hyperfine tensors by simulation of ENDOR X-band spectra measured across the EPR envelope allows us to characterize the Fe–N bonding and to describe the orientation of the Fe–N bonds with respect to the g tensors. Figure 3 shows the ν_+ feature of the two ^{15}N doublets recorded at various positions along the EPR envelope; the ν_- partners (not shown) give an identical pattern at a frequency lower by $2\nu(^{15}N)$ = 3.1 MHz. The single-crystal-like ENDOR spectrum taken at g_1 = 2.01 shows two sharp ν_+ peaks, one from each of two coordinated ^{15}N. As the g value is decreased to g_2, these two sharp resonances shift to lower frequency, and a shoulder appears on the high-frequency edge of the pattern. The breadth of the ν_+ ENDOR pattern reaches its maximum

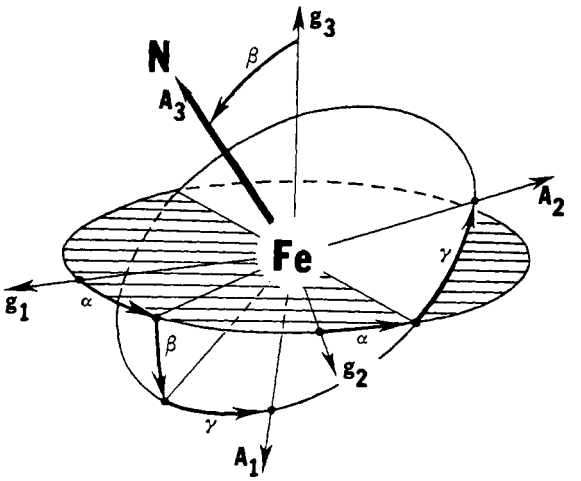

FIGURE 4: Definition of the Euler angles (α, β, γ) relating nitrogen hyperfine coupling tensor **A** to **g** coordinate frame.

at g_2 (Figure 3). As the observing g value is further decreased (field increased) to g_3 = 1.76, the two sharp resonances move back toward higher frequency, and the shoulder retreats to lower frequency, until at g_3 the single-crystal-like ENDOR pattern reveals only one broad peak.

The principal values and relative orientations of the hyperfine coupling tensors for the two ^{15}N ligands have been determined from simulations of the full set of ENDOR spectra following the procedures described by True et al. (1988). The tensors were first treated as being coaxial with the g tensor; approximations to A_1 (along g_1) and A_3 (along g_3) were obtained from the ENDOR frequencies measured in the single-crystal-like spectra obtained respectively at the high- and low-field edge of the EPR envelope. For the N(1) site, A_2 was estimated from the position of the single sharp ν_+ resonance observed at g_2; for the N(2) site, A_2 was estimated from the breadth of the g_2 pattern as well as the peak positions. Then the variation of the ENDOR patterns was matched by varying the orientation of **A** with respect to **g**, while adjusting the A_i so as to reproduce the resonance frequencies in the single-crystal-like spectra. The relationship between coordinate frames is presented in Figure 4. Because the weaker shoulders for N(1) are overlapped by the strong N(2) peak, the value of A_2 for the N(1) site was determined only by reproducing the position of the single sharp ν_+ resonance seen at g_2; however, it is clear that the calculated and observed spectra match closely throughout the EPR envelope (Figure 3).

For both ^{15}N sites simulations that employed coaxial tensors or rotations of $\mathbf{A}^N$ around only the g_3 axis ($\alpha \neq 0$) failed to reproduce either (i) the shift of the two sharp doublets to lower rf frequency as g_{obs} was decreased from g_1 to g_2 or (ii) the breadth of the ENDOR pattern seen at g_2. Rotations around the g_2 axis ($\beta \neq 0$) did reproduce this shift, as well as the subsequent retreat of the two sharp resonances to higher frequency as g_{obs} is decreased further, $g_2 > g > g_3$. Furthermore, extra ENDOR peaks that split off from the resonances and moved to higher frequency match the shoulders seen at the intermediate, non-single-crystal-like fields (Figure 3). Spectra at all observing fields could be simulated with the hyperfine tensors given in Table I, in particular with β = 35° (±5°) for site 1 and β = 50° (±5°) for site 2. As seen in the selected data presented in Figure 3, the simulations fully reproduce the positions of the two sharp resonances, as well as the breadth of the pattern to higher frequency and other resolved features. Figure 5 is a plot of the calculated and observed ENDOR frequencies versus the observing g value (static field) and shows in detail the agreement between experimental

Table I: Hyperfine and Quadrupole Tensor Principal Values (MHz) and Orientations (deg) Relative to g Tensor Principal Axes for the Histidyl-Nitrogen Ligands to the [2Fe-2S] Cluster of Phthalate Dioxygenase from *P. cepacia*[a] and to the Heme of Met-Mb[b]

	principal values		
	site 1	site 2	met-Mb
A(^{15}N)			
A_1	4.6(2)	6.4(1)	−11.31(6)
A_2	5.4(1)	7.0(1)	−11.66(6)
A_3	8.1(1)	9.8(2)	−16.17(15)
P(^{14}N)			
P_1	0.85(8)	0.80(8)	0.81(6)
P_2	0.45(8)	0.35(8)	0.31(6)
P_3	−1.3	−1.15	−1.12(6)
Euler angles[c]			
α	0(30)	0(10)	
β	35(5)	50(5)	
γ	0(10)	0(30)	

[a] This work. The absolute signs of the A_i are not determined; for an individual site, all have the same sign. The relative signs of the P_i are determined by simulations that use $A(^{14}N) = [g(^{14}N)/g(^{15}N)]A(^{15}N)$; the absolute signs come from comparison with those of met-Mb. Uncertainties in last significant figure are listed in parentheses. P_3 has no listed uncertainty because it is calculated from $P_1 + P_2 + P_3 = 0$. [b] Scholes et al. (1982). The tabulated $A_i(^{15}N)$ were calculated from the published $A_i(^{14}N)$ with eq 3, and the labeling of the tensor components has been made to conform with ours. [c] Euler angles relate the A tensor to the reference g frame; they are discussed under Procedures and Theory and defined in Figure 4. The values for the fitting parameters α and β were determined by fitting ^{15}N ENDOR data. The quadrupole and hyperfine tensors are assumed coaxial, and γ was determined by fitting the ^{14}N data. See text.

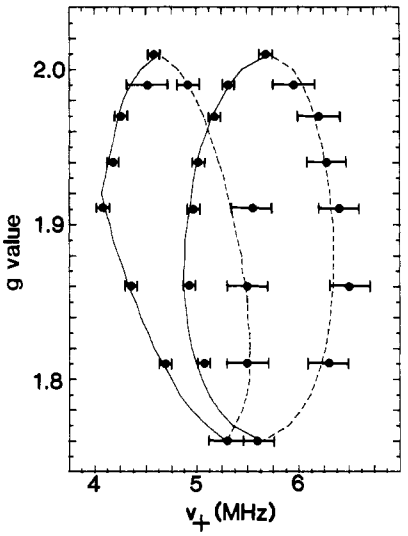

FIGURE 5: Plot of the frequency of the ENDOR features for ν_+ versus the observing g value (static field). The theoretical values, calculated with the hyperfine tensor parameters given in Table I, are indicated as solid lines for resolved peaks and dotted lines for shoulders.

and theoretical positions for the ENDOR peaks of both ^{15}N sites.

For neither site were the simulations particularly sensitive to the angle α that defines the orientation of the Fe–N bond with respect to the g_1–g_3 plane; relative orientations of $0 \leq |\alpha| \leq 30°$ for both sites could be accommodated without any visible changes in the simulated ^{15}N ENDOR pattern, provided corresponding minor modifications were made in the A_i. However, a value of α in the vicinity of 90° is not permitted in either case. Moreover, ^{14}N analyses presented below require $0 \leq |\alpha(2)| \leq 10°$. Crystal field analysis of the g tensors of [2Fe-2S] clusters has raised the question as to the orientation of the g tensor axes with respect to the plane containing the four protein ligands to the cluster (Bertrand et al., 1985). The present data clearly indicate that the ligand plane most closely corresponds with the g_1–g_3 plane.

The two ^{15}N tensors have nearly axial symmetry with the unique axis assigned to the Fe–N bond. Thus, simulations should not be influenced by rotations of the tensor about this bond, as described by the angle γ, and this is the case.

Analysis of Fe–^{15}N Bonding. Analysis of the isotropic and the anisotropic components of the hyperfine coupling confirms that both nitrogens are coordinated to iron and can be used to characterize the bonding. The hyperfine tensors for N(1) and N(2) both are effectively of axial symmetry (Table I). The anisotropic component can have contributions from spin density in the 2p orbital on nitrogen as well as from direct dipolar interaction with the Fe^{2+} ($S = 2$) ion. In either case the unique tensor direction corresponds to the N–Fe vector. For both ligands, the unique tensor component (A_3) has a magnitude considerably larger than those of A_1 and A_2. We can rule out the possibility that the coupling arises solely from a through-space dipolar interaction (Atherton, 1973) without covalent Fe–N bonding; this would give $A_1 = A_2 = (-A_3)/2$. However, the ENDOR simulations require that all A_i have the same sign.[4] Moreover, the magnitudes of the A_i are more than 5-fold greater than could arise from dipolar interactions (see below). Thus, the two ^{15}N tensors have a considerable isotropic component [$A_{iso} = (1/3)\sum A_i$; $A_{iso}(1) = 6$ MHz; $A_{iso}(2) = 7.7$ MHz] that arises from s orbital density on the two nitrogens, which proves that they are covalently bonded to Fe. The fact that the couplings for the two nitrogens are similar in magnitude proves that they are associated with two different histidines directly coordinated to iron, and not with the coordinated and remote nitrogen of a single such ligand: the magnitude of the hyperfine coupling to the remote nitrogen of a metal-coordinated histidyl imidazole is reduced by more than 20-fold from that of the coordinated nitrogen.[5]

The $\mathbf{A}(i)$ tensors, $i = 1$ or 2, of Table I are defined in terms of the nuclear hyperfine interaction with the total spin, $S = {}^1/_2$, of the spin-coupled [Fe^{3+},Fe^{2+}] pair. The spin-coupling model of Gibson et al. (1966) can be used to relate these tensors to the fundamental hyperfine tensors, $\mathbf{a}(i)$, that describe the interaction of nitrogen with the spin of the isolated Fe^{2+} ion:[6]

$$\mathbf{a} = -3\mathbf{A}/4$$

Justification for taking both ligands to be coordinated to Fe^{2+} is given below (for coordination to Fe^{3+} the relation is $\mathbf{a} = 3\mathbf{A}/7$). The isotropic component of the hyperfine coupling, $a_{iso} = -3A_{iso}/4$, is related to f_s, the fraction of unpaired electron spin that resides in the 2s orbital by

$$a_{iso} = \frac{f_{2s}a^\circ_{2s}}{2S} \qquad (5)$$

where $a^\circ_{2s} = 1163$ MHz is the coupling for unit spin population (Morton & Preston, 1978) and $S = 2$ for ligation to the ferrous ion site. Using eq 5 and the data in Table I, we calculate $f_{2s}(1) \approx 1.5\%$ and $f_{2s}(2) \approx 2\%$. The only available comparison for histidine coordinated to iron is with the axial ligand to the high-spin Fe^{3+} ion of aquometmyoglobin, where

[4] However, the measurements do not give the absolute signs of the A_i (Atherton, 1973).

[5] This has been demonstrated directly for imidazole bonded to Cu^{2+} (van Camp et al., 1981; Mims & Peisach, 1978; Roberts et al., 1984) and may be inferred for imidazole bonded to Fe^{3+} from the work of Scholes et al. (1982).

[6] This procedure was applied to ^{57}Fe ENDOR measurements on [2Fe-2S] ferredoxins by Sands and Dunhan (1975).

a similar value, $f_{2s} \approx 3\%$ (Scholes et al., 1982), is found.

The anisotropic part of the ^{15}N hyperfine coupling has a local contribution, a_{2p}, that arises from unpaired density in the 2p orbital on nitrogen (f_{2p}) and from direct dipolar coupling to the ferrous ion, a_{3d}. Idealizing the hyperfine tensors as having axial symmetry, then

$$a_3 \approx a_{iso} + 2a_{2p} + 2a_{3d} \quad (6)$$

where

$$a_{2p} = \frac{f_{2p}a^\circ_{2p}}{2S} \quad (7a)$$

and the point-dipole approximation, which overestimates the dipolar coupling, gives

$$a_{3d} \approx \frac{f_{Fe}g_e g(^{15}N)\beta_e\beta_N}{R^3} \quad (7b)$$

Here the fraction of the spin residing on the ferrous ion is reduced from unity to f_{Fe} by delocalization onto its ligands, $a^\circ_{2p} = 67.2$ MHz is the ^{15}N hyperfine coupling for unit spin in a nitrogen 2p orbital, and R is the Fe–N bond length. A value of $R \approx 2.2$ Å yields $2a_{3d} \sim 1.5f_{Fe}$ MHz and $2a_{2p} + 2a_{3d} \sim 1.6$ MHz for both $^{15}N(1)$ and $^{15}N(2)$. Taking the value $f_{Fe} \sim 0.8$ suggested by calculations on [2Fe-2S] clusters (Noodleman & Baerends, 1984) leads to $a_{2p} \sim 0.2$ MHz and $f_{2p} \gtrsim 1\%$ for both ^{15}N ligands. This approximate analysis of the ^{15}N hyperfine constants nonetheless is encouragingly self-consistent in that $f_{2p}/f_{2s} \sim 1$, which is reasonable for the sp^n hybrid of an imidazole nitrogen (Brown & Hoffman, 1980; Scholes et al., 1982).

Analysis of ^{14}N ENDOR Spectra and Determination of ^{14}N Quadrupole Tensors. The analysis of the two ^{15}N hyperfine tensors gives the corresponding ^{14}N tensors through eq 3. This knowledge along with the enhanced resolution of the ^{14}N ENDOR patterns from PDO with [^{14}N]histidine in a ^{15}N background (sample 4; Figure 2C) gives us the further opportunity to analyze the ^{14}N spectra and to determine the ^{14}N quadrupole coupling tensors. This determination permits us to define the orientation of the histidine rings with respect to the NFeN plane and gives the quadrupole tensor components, which are additional bonding parameters.

^{14}N ENDOR spectra of sample 4 were recorded at various positions along the EPR envelope at Q-band frequency. The ν_+ features (eq 1) are presented in Figure 6. The starting point for simulating these spectra was as follows. (1) The principal values of $\mathbf{A}(^{14}N)$ were calculated from those of the $\mathbf{A}(^{15}N)$ with eq 3. (2) The **A** and **P** tensors were taken as coaxial; because **A** is essentially axial, this corresponds to assigning a principal axis of **P** to lie along A_3. This assumption is valid for the histidine coordinated to Fe^{3+} in metmyoglobin (Scholes et al., 1982). (3) The Euler angles α and β given in Table I were used. (4) The principal values of the quadrupole tensor were taken to be the same for N(1) and N(2). (5) Finally, the quadrupole tensor is traceless, $P_1 + P_2 + P_3 = 0$ (Abragam & Bleaney, 1970). With these restrictions the ^{14}N simulations depend on four unknown parameters: two principal values of **P**, namely, P_1 and P_2, and $\gamma(1)$ and $\gamma(2)$, the rotations of the two tensors about their Fe–N bond.

The process was initiated by assigning the single-crystal-like $\nu_{+,m}(^{14}N)$ spectrum at g_1 (Figure 6) from the corresponding $\nu_+(^{15}N)$ spectrum (Figure 3). Insertion of the $\nu_+(^{15}N)$ transition frequencies at X-band (Figure 3; 5.6 and 4.55 MHz) into eq 3 and 1 predicts that the $\nu_+(^{14}N)$ transitions at Q-band should be pairs of lines centered at 6.9 and 6.2 MHz and split by the quadrupole interaction. Examination of Figure 6 for

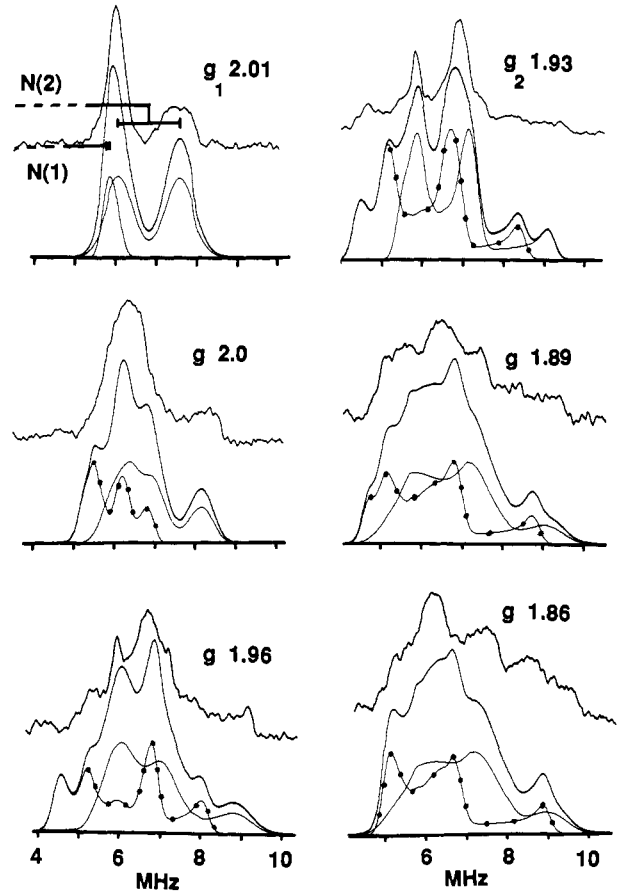

FIGURE 6: ^{14}N ENDOR spectra of PDO (sample 4) showing the ν_+ resonances at selected magnetic fields. Computer simulations that employ the parameters listed in Table I are shown below the corresponding spectra. Simulations for the individual ^{14}N plus their sum are shown; the curves for N(1) are indicated by (●). The ENDOR line widths were taken as 0.2 and 0.5 for N(1) and N(2), respectively, independent of orientation except at g_2, where a line width of 0.2 MHz was used for both; relative amplitudes were adjusted for best fit. See legend to Figure 3.

$g = g_1$ yields quadrupole splittings of $3P_{obs}$ of ~1.5 MHz for N(2) and ≲0.2 MHz for N(1). Initially taking $\gamma(1) = \gamma(2) = 0$, a set of $[P_1,P_2]$ values that reproduced P_{obs} for each ligand at g_1 was determined. For a given value of the splitting at g_1, this set is a straight line[7] in a plot of P_1 vs P_2; taking into account uncertainties in peak positions for each ^{14}N, the possible $[P_1,P_2]$ pairs are encompassed by a narrow band of points flanking the lines plotted in Figure 7. On the assumption that the principal values of **P** for the two ^{14}N are the same, then the region near the intersection of the lines for N(1) and N(2), of extent ca. ±0.1 MHz in P_1 and P_2, constituted a set of trial values for $[P_1,P_2]$ (Figure 7). Parameter

[7] The linear relation between P_2 and P_1 arises because the equation for the angle-dependent quadrupole splitting parameter is linear in the P_i (Thuomas & Lund, 1972); it is given by

$$P_2 = \frac{C_1}{C_2}P_1 + \frac{C_2}{g^2A^2}P_{obs}$$

where

$$C_1 = (\tilde{I}\cdot{}^s\tilde{A}\cdot\mathbf{U}_3\cdot{}^s\mathbf{A}\cdot I) - (\tilde{I}\cdot{}^s\tilde{A}\cdot\mathbf{U}_1\cdot{}^s\mathbf{A}\cdot I)$$

$$C_2 = (\tilde{I}\cdot{}^s\tilde{A}\cdot\mathbf{U}_2\cdot{}^s\mathbf{A}\cdot I) - (\tilde{I}\cdot{}^s\tilde{A}\cdot\mathbf{U}_3\cdot{}^s\mathbf{A}\cdot I)$$

$$\mathbf{U}_1 = \tilde{\mathbf{M}}\begin{pmatrix}1&0\\0&0\end{pmatrix}\mathbf{M} \qquad \mathbf{U}_2 = \tilde{\mathbf{M}}\begin{pmatrix}0&1\\0&0\end{pmatrix}\mathbf{M} \qquad \mathbf{U}_3 = \tilde{\mathbf{M}}\begin{pmatrix}0&0\\0&1\end{pmatrix}\mathbf{M}$$

and other symbols are defined in True et al. (1988).

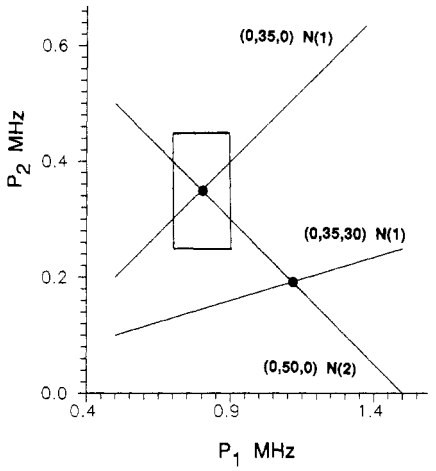

FIGURE 7: Plot of P_1 vs P_2 such that the pair of values yields the quadrupole splitting of 0 and 1.5 MHz for N(1) and N(2), respectively, at g_1. The lines are calculated with the equation in footnote 7 using ^{14}N hyperfine tensors calculated from the ^{15}N tensors in Table I. The numbers in the parentheses are the Euler angles α, β, and γ. The intersection points represent values of P_1 and P_2 such that the two nitrogens have identical quadrupole coupling tensor principal values. The box represents the range of uncertainty in determining the intersection point due to the uncertainty of ±0.1 MHz in measuring the quadrupole splitting for N(1) and N(2) at g_1. Note the difference in scale for the abscissa and ordinate.

pairs within this region were next tested to see if they could reproduce the overall spread of the pattern observed at g = 1.92 (Figure 6). Further selection of the best parameter sets involved simulations of ENDOR spectra at multiple fields. This procedure was then repeated over a grid of values for $[\gamma(1),\gamma(2)]$, thereby determining the ranges of the parameters $[P_1,P_2,\gamma(1),\gamma(2)]$ that yielded the best fits. Finally, the requirement that the two quadrupole tensors be identical was relaxed, and further simulations were done; these simulations in addition explored a grid of $[\alpha(1),\alpha(2)]$ values, $0 \leq |\alpha(i)| \leq 30°$. The parameters best reproducing the experiments are listed in Table I, and the simulations are shown in Figure 6.

The simulations reproduce the observations in a quite reasonable manner, particularly for $g \geq g_2$, where the experimental signal/noise is best. It is noteworthy that the tensor values *independently* arrived at are almost identical with those for the axial histidine bound to the heme of aquomet-Mb (Table I).[8] In particular, the components along the Fe–N bonds, P_3, correspond, as they should. Because of this agreement, we assume that we may use the Mb results to deduce the physical orientation of the imidazole planes in PDO relative to the quadrupole axes. In Mb, the tensor component perpendicular to this plane is P_2 = 0.31 (Scholes et al., 1982); we assign the same for PDO. Thus, for α = 0 the parameter γ corresponds to the dihedral angle between the imidazole and the g_1–g_3 planes, with the latter corresponding to the N(1)-FeN(2) plane.

Is There Another Nitrogenous Ligand? It was shown earlier for ^{14}N Rieske-type clusters that when the magnetic field is set to g_3, the X-band ENDOR pattern in the range 10–22 MHz is not symmetric about $\nu_H \sim 16$ MHz as would be expected for proton resonances (Cline et al., 1985; Telser et al., 1987). This led us to assign a feature in the 13–14-MHz region to a strongly coupled nitrogen ligand of the Rieske-type

[8] Because of the agreement, we do not include an analysis of the P_i in terms of bonding parameters, which would follow the procedures of Brown and Hoffman (1980) and Scholes et al. (1982) and give results indistinguishable from those for histidine in the latter.

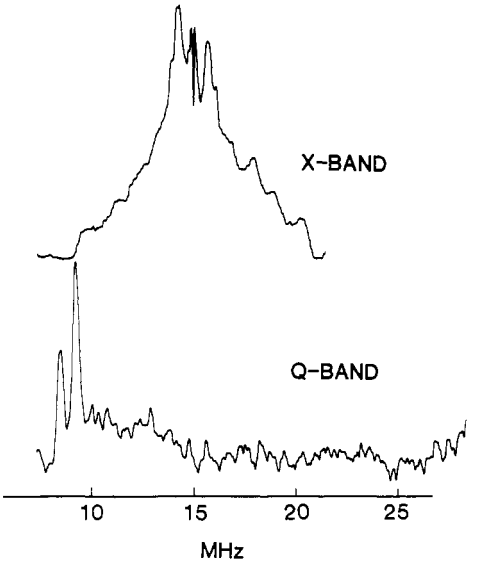

FIGURE 8: ENDOR spectra at X-band and Q-band microwave frequencies of ^{15}N-enriched PDO from *P. cepacia* (sample 2), both taken at g_2 = 1.92. Conditions: T = 2 K; microwave frequency, 9.6 (X-band) and 35.3 GHz (Q-band); microwave power, 10 (X-band) and 50 μW (Q-band); 100-kHz field modulation, 1 G; rf power, 20 W; rf scan rate, 1.0 (X-band) and 2.5 MHz/s (Q-band); 500 scans.

[2Fe-2S] center with $A(^{14}N)/2 \sim$ 13–14 MHz. ENDOR experiments at Q-band frequencies now rule out this interpretation and show that there is no nitrogenous ligand other than the two histidines discussed above.

At Q-band the proton ENDOR resonances at g = 1.9 are centered at $\nu_H \sim 51$ MHz, rather than at $\nu_H \sim 15$ MHz as at X-band. Because the ^{14}N and ^{15}N resonances are centered at $A(N)/2$ and do not shift with microwave frequency, this allows for the examination of nitrogen signals in the region of 0–40 MHz without interference from proton signals. Figure 8 shows X-band and Q-band ENDOR spectra taken at g_2 = 1.92 for ^{15}N-enriched PDO samples. If there were a ligand with $A(^{14}N)/2 \sim$ 12–14 MHz, then (by eq 1 and 2) at Q-band the ^{15}N ENDOR pattern would be a doublet with $\nu_- \sim 14$ and $\nu_+ \sim 23$ MHz. From the Q-band spectrum it is clear that there is no such strongly coupled ^{15}N signal in this region.

The ^{15}N resonances at ν_+ = 8.2 and 9.2 MHz in Figure 2, curve B (sample 2), correspond to those observed at ν_+ = 4.1 and 4.85 MHz in the X-band ENDOR spectrum (Figure 1). The absence of high-frequency ^{15}N signals in a trace that contains ^{15}N resonances at 8–9 MHz is highly significant. If there were resonances at ~19 and 23 MHz, their ENDOR intensity would be much greater than that for the two readily observed low-frequency peaks in Figure 2, curve B, because ENDOR intensity in general scales as the square of the resonance frequency (Atherton, 1973).

With the possibility of a high-frequency nitrogen resonance eliminated, we reexamined the proton resonances of PDO. Figure 9 presents proton ENDOR spectra of [^{14}N]- and [^{15}N]PDO recorded at various g values across the EPR envelope. To permit comparison of spectra recorded at X- and Q-bands, each abscissa is labeled in terms of the ENDOR shift, $\delta\nu = \nu - \nu_H$.

The wings of the spectrum at g_3 = 1.76 for the ^{14}N sample are asymmetric, with greater intensity for $\delta\nu < 0$ than for $\delta\nu > 0$ MHz as reported by Cline et al. (1985). However, at other g values, for example, g = 1.86, the proton ENDOR patterns for [^{14}N]PDO are more nearly symmetric. At all magnetic fields, substitution with ^{15}N results in a proton pattern that more nearly approaches the expected symmetric shape. It has been shown that protons can give highly asym-

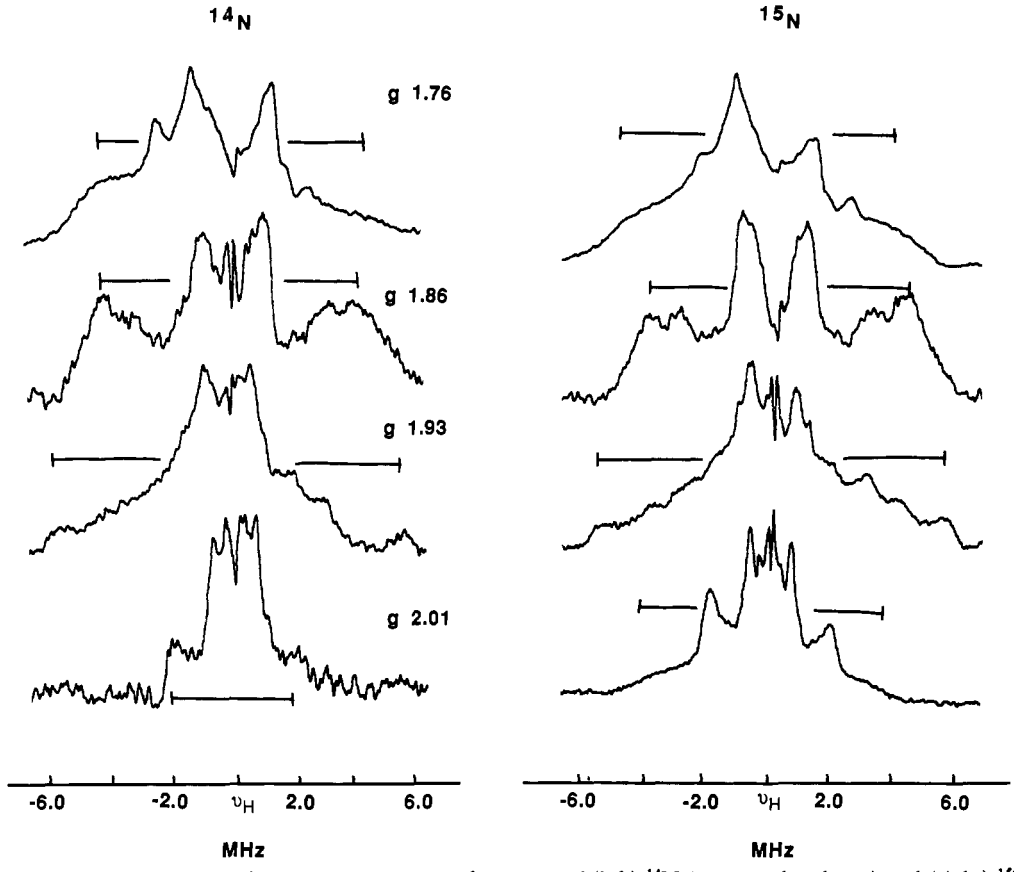

FIGURE 9: Proton ENDOR spectra centered at the proton Larmor frequency of (left) ^{14}N (natural abundance) and (right) ^{15}N-enriched PDO samples from *P. cepacia* at various g values as indicated. Both spectra at $g = 1.76$ and that of [^{15}N]PDO at $g = 2.01$ were recorded at Q-band frequency; all others were at X-band frequency. The fiducial marks indicate the largest splittings. Conditions: $T = 2$ K, microwave frequency, 9.6 (X-band) and 35.3 GHz (Q-band); microwave power, 10 (X-band) and 50 μW (Q-band); 100-kHz field modulation, 1 (X-band) and 3.2 G (Q-band); rf power, 20 W; rf scan rate, 1.0 MHz/s; 500 scans.

metric patterns when there is strong cross-relaxation by ^{14}N nuclei (Hass et al., 1983; Lubitz & Nyronen, 1980); it was further shown that enrichment with ^{15}N reduces this asymmetry. The results presented in Figure 9 suggest that such a mechanism plays a role in determining the proton ENDOR patterns for PDO.

Site of Histidine Ligation. The data from Mössbauer spectroscopy (Fee et al., 1984) suggested that the two non-cysteine ligands to the [2Fe-2S] cluster of *Thermus* Rieske protein are coordinated to the ferrous site, and such unsymmetrical coordination is consistent with the Raman measurements (Kuila et al., 1987). However, the Mössbauer data could not rule out ligation to different iron sites if the two non-cysteine ligands were very dissimilar. The determination by ENDOR spectroscopy that two ligands coordinated to the cluster are nitrogens from histidine and that these have similar hyperfine parameters indicates that both are bonded to Fe^{2+}.

Structure of the Cluster. The analysis of the ^{15}N ENDOR data indicates that the NFeN and g_1–g_3 planes correspond (Table I; $\alpha \approx 0$). This leads to a geometric model (Figure 10) in which the four protein-donated ligands and two iron ions lie in the g_1–g_3 plane with either g_3 or g_1 lying along the Fe–Fe vector. With the former assignment the angle between Fe–N and Fe–Fe vectors is β, and the bite angle subtended by the two Fe–N vectors is $\beta(1) + \beta(2) \sim 85°$ ($\pm 10°$). This assignment is favored by a crystal-field analysis of the g values for [2Fe-2S] clusters with $g_{av} \sim 1.91$ (Bertrand et al., 1985). In contrast, if the Fe–Fe vector corresponds to g_1, as appears to be the case for ordinary [2Fe-2S] ferredoxins with $g_{av} \sim 1.96$, then the angle between Fe–N and Fe–Fe vectors is $\bar{\beta} = (\pi/2) - \beta$, and the bite angle is $\bar{\beta}(1) + \bar{\beta}(2) \sim 95°$ ($\pm 10°$).

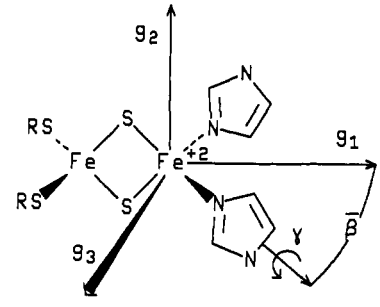

FIGURE 10: Structure of the Rieske-type [2Fe-2S] cluster of PDO as determined by ENDOR spectroscopy. The [2Fe-2S] core and the g_1–g_2 plane lie in the paper. The angles γ and β, with $\bar{\beta} = (\pi/2) - \beta$, are given in Table I.

Because the slightly larger bite angle seems more attractive, the latter assignment has been used in Figure 10; however, ^{57}Fe ENDOR studies or single-crystal measurements will be required for a final determination. In either case, the torsion angle twisting an imidazole about the Fe–N bond and out of the NFeN plane is γ, which appears to be relatively small for both of the histidines (Table I). A companion paper (Tsang et al., 1989) complements these results through the determination of Fe–S and Fe–N bond lengths by EXAFS measurements.

The resulting geometry at Fe^{2+}, if *idealized*, would have tetrahedral coordination with the two histidyl imidazoles lying within the NFeN plane. Although this idealized geometry would have unacceptably short contacts between the two imidazoles, the range of acceptable values for the $\alpha(i)$, $\beta(i)$, and especially $\gamma(i)$, $i = 1$ and 2, easily is sufficient to permit a reasonable geometry. Indeed, the simple observation that the

quadrupole splittings observed at g_1 differ sharply for N(1) and N(2) (Figure 6), although the principal values do not, by itself demonstrates that the geometry at Fe^{2+} is *not* ideally symmetric; in our fits this is indicated by the different values of β and is further allowed by the appreciable uncertainties in the α and γ angles.

Interestingly, although the same ENDOR line widths can be used to describe the spectra for $^{15}N(1)$ and $^{15}N(2)$ (Figure 3), this is not so for $^{14}N(1)$ and $^{14}N(2)$; this can be seen immediately in the spectrum at g_1, where the line width for $^{14}N(2)$ is greater than that for $^{14}N(1)$ (Figure 6). We interpret this to mean that histidine 2 has a greater conformational mobility than histidine 1 when the protein is in fluid solution, and that this leads to a distribution in values of $\gamma(2)$ in the frozen solutions under study; this distribution causes a spread in quadrupole splittings and an apparent increase in line width. The absence of any effects of the $\gamma(2)$ distribution on the ^{15}N spectra is a consequence of the axial symmetry of the hyperfine tensors and the invariance of the spectra to rotations about the Fe–N bond (angle γ).

Summary

(1) The use of 9- and 35-GHz ENDOR spectroscopy on selectively ^{15}N-enriched phthalate dioxygenase protein samples prepared from wild-type *P. cepacia* and histidine auxotrophs has unequivocally demonstrated that two imidazole nitrogens from histidine residues are coordinated to Fe of the Rieske [2Fe-2S] cluster. This is in contrast to the classical ferredoxin-type [2Fe-2S] centers in which all ligation is by sulfur of cysteine residues. No other nitrogen couplings to the iron cluster were revealed by ENDOR.

(2) The combination of data from ENDOR, Mössbauer, and Raman spectroscopies indicates that both histidines are coordinated to the Fe^{2+} site of the reduced cluster.

(3) The ^{15}N hyperfine tensor for each coordinated nitrogen has been determined (Table I). Analysis of these tensors shows that each can be reasonably interpreted in terms of an sp^n hybrid orbital on histidyl nitrogen coordinated to Fe^{2+}. Analysis of the ^{14}N ENDOR spectra shows the quadrupole tensors for the two ^{14}N ligands to be nearly identical with those of the histidine ^{14}N coordinated to the heme iron of met-Mb.

(4) The orientations of the **A** and **P** tensors relative to the *g* tensor are consistent with roughly tetrahedral coordination at Fe^{2+}. The ligand plane as defined by the two Fe and the coordinating N atoms provided by the protein is found to correspond to the g_1–g_3 plane. The analyses suggest that the dihedral twist of the two imidazole rings relative to the NFeN plane, which causes the ligands to look like propeller blades, is relatively small for both.

(5) Evidence is presented that in fluid solution the two histidines have different conformational mobilities.

(6) Because the ^{14}N and ^{1}H ENDOR patterns, as well as other spectroscopic properties, for the *Thermus* and mitochondrial Rieske proteins are virtually indistinguishable from those of PDO (Cline, et al., 1985; Telser et al., 1987),[9] we infer that the structure presented here is generally applicable to Rieske-type centers.

Acknowledgments

We acknowledge William R. Ranger for help in early phases of this work and Dr. Debasish Kuila for assistance in some sample preparations.

[9] Unpublished results.

Registry No. PDO, 63626-44-8; N, 7727-37-9; Fe, 7439-89-6; L-His, 71-00-1.

References

Abragam, A., & Bleaney, B. (1970) *Electron Paramagnetic Resonance of Transition Ions*, Clarendon, Oxford.

Albracht, S. P. J., & Subramanian, J. (1977) *Biochim. Biophys. Acta 462*, 36–48.

Atherton, N. M. (1973) *Electron Spin Resonance*, Wiley, New York.

Batie, C. J., LaHaie, E., & Ballou, D. P. (1987) *J. Biol. Chem. 262*, 1510–1518.

Bernhardt, F.-H., & Ruf, H.-H. (1974) *FEBS Lett. 43*, 53–55.

Bertrand, P., Guigliarelli, B., Gayda, J.-P., Beardwood, P., & Gibson, J. F. (1985) *Biochim. Biophys. Acta 831*, 261–266.

Brown, T. G., & Hoffman, B. M. (1980) *Mol. Phys. 39*, 1073–1109.

Bull, C., & Ballou, D. P. (1981) *J. Biol. Chem. 256*, 12673–12680.

Cline, J. F., Hoffman, B. M., Mims, W. B., LaHaie, E., Ballou, D. P., & Fee, J. A. (1985) *J. Biol. Chem. 260*, 3251–3254.

Cramer, W. A., Widger, W. R., Black, M. T., & Girven, M. E. (1987) *Topics in Photosynthesis* (Barber, J., Ed.) Vol. 8, *The Light Reactions*, pp 447–493, Elsevier Medical Press, New York.

Degli Esposti, M., Ballester, F., Solaini, G., & Lenaz, G. (1987) *Biochem. J. 241*, 285–290.

Fee, J. A., Findling, K. L., Yoshida, T., Hille, R., Tarr, G. E., Hearshen, D. O., Dunham, W. R., Day, E. P., Kent, T. A., & Münck, E. (1984) *J. Biol. Chem. 259*, 124–133.

Fee, J. A., Kuila, D., Mather, M. W., & Yoshida, T. (1986) *Biochim. Biophys. Acta 853*, 153–185.

Geary, P. J., Saboowalla, F., Patil, D., & Cammack, R. (1984) *Biochem. J. 217*, 667–673.

Gibson, J. F., Hall, D. O., Thornley, J. H. M., & Whatley, F. R. (1966) *Proc. Natl. Acad. Sci. U.S.A. 56*, 987–990.

Hass, Ch., Kirste, B., Kurreck, K. H., & Schlömp, G. (1983) *J. Am. Chem. Soc. 105*, 7375–7383.

Hauska, G., Hurt, E., Gabellini, N., & Lockan, W. (1983) *Biochim. Biophys. Acta 726*, 97–133.

Hoffman, B. M., Martinsen, J., & Venters, R. A. (1984) *J. Magn. Reson. 59*, 110–123.

Hoffman, B. M., Martinsen, J., & Venters, R. A. (1985) *J. Magn. Reson. 62*, 537–542.

Iwasaki, M. (1974) *J. Magn. Reson. 16*, 417–423.

Kuila, D., Fee, J. A., Schoonover, J. R., Batie, C. J., Ballou, D. P., & Woodruff, W. H. (1987) *J. Am. Chem. Soc. 109*, 1559–1561.

Lubitz, W., & Nyrönen, T. (1980) *J. Magn. Reson. 41*, 17–29.

Malkin, R., & Bearden, A. J. (1978) *Biochim. Biophys. Acta 505*, 147–181.

Mathews, J., & Walker, R. L. (1965) *Mathematical Methods of Physics*, W. A. Benjamin, New York.

Mims, W. B., & Peisach, J. (1978) *J. Chem. Phys. 69*, 4921–4930.

Morton, J. R., & Preston, K. F. (1978) *J. Magn. Reson. 30*, 577–582.

Noodleman, L., & Baerends, E. J. (1984) *J. Am. Chem. Soc. 106*, 2316–2327.

Olsen, R. H., & Shipley, P. (1973) *J. Bacteriol. 113*, 772–780.

Palmer, G., Tsai, A.-L., Kauten, R., Degli Esposti, M., & Lenaz, G. (1985) *Achievements and Perspectives of Mitochondrial Research* (Quagliariello, E., Ed.) Vol. I, *Bioenergetics*, pp 137–146, Elsevier Science, Amsterdam.

Rieske, J. S. (1976) *Biochim. Biophys. Acta 456*, 195–247.

Rieske, J. S., MacLennan, D. H., & Coleman, R. (1964a) *Biochem. Biophys. Res. Commun. 15*, 338-344.
Rieske, J. S., Zaugg, W. S., & Hansen, R. E. (1964b) *J. Biol. Chem. 239*, 3023-3030.
Rist, G. H., & Hyde, J. S. (1970) *J. Chem. Phys. 52*, 4633-4643.
Roberts, J. E., Cline, J. F., Lum, V., Freeman, H., Gray, H. B., Peisach, J., Reinhammer, B., & Hoffman, B. M. (1984) *J. Am. Chem. Soc. 106*, 5324-5330.
Sands, R. H., & Dunham, W. R. (1975) *Q. Rev. Biophys. 7*, 443-504.
Scholes, C. P., Lapidot, A., Mascarenhas, R., Inubushi, T., Isaacson, R. A., & Feher, G. (1982) *J. Am. Chem. Soc. 104*, 2724-2735.
Siedow, J., Power, S., De la Rosa, F. F., & Palmer, G. (1978) *J. Biol. Chem. 253*, 2392-2399.
Tarr, G. E. (1986) *Methods of Protein Microcharacterization* (Shively, J. E., Ed.) pp 155-194, Humana Press, Clifton, NJ.
Telser, J., Hoffman, B. M., LoBrutto, R., Ohnishi, T., Tsai, A.-L., Simpkin, D., & Palmer, G. (1987) *FEBS Lett. 214*, 117-121.
Thuomas, K.-A., & Lund, A. (1974) *J. Magn. Reson. 18*, 12-21.
True, A. E., Nelson, M. J., Venters, R. A., Orme-Johnson, W. H., & Hoffman, B. M. (1988) *J. Am. Chem. Soc. 110*, 1935-1943.
Trumpower, B. L. (1981a) *Biochim. Biophys. Acta 639*, 129-155.
Trumpower, B. L. (1981b) *J. Bioenerg. Biomembr. 13*, 1-24.
Trumpower, B. L., & Edwards, C. A. (1979) *J. Biol. Chem. 254*, 8697-8706.
Tsang, H.-T., Batie, C. J., Ballou, D. P., & Penner-Hahn, J. E. (1989) *Biochemistry* (in press).
Van Camp, H. L., Sands, R. H., & Fee, J. A. (1981) *J. Chem. Phys. 75*, 2098-2107.
Venters, R. A., Nelson, M. J., McLean, P., True, A. E., Levy, M. A., Hoffman, B. M., & Orme-Johnson, W. H. (1986) *J. Am. Chem. Soc. 108*, 3487-3498.
Zylstra, G. J. (1987) Ph.D. Dissertation, The University of Michigan.

Occurrence and Inducibility of Cytochrome P450IIIA in Maternal and Fetal Rats during Prenatal Development†

Janis E. Hulla and Mont R. Juchau*
Department of Pharmacology, SJ-30, University of Washington School of Medicine, Seattle, Washington 98195
Received November 4, 1988; Revised Manuscript Received January 17, 1989

ABSTRACT: The purpose of this study was to quantify cytochrome P450IIIA1 in fetal and maternal livers of uninduced and pregnenolone-16α-carbonitrile (PCN) induced rats during the course of prenatal development. The activities and levels of P450IIIA in hepatic microsomes from maternal rats and fetuses at 15-21 days of gestation were measured by triacetyloleandomycin (TAO) inhibited debenzylation of (benzyloxy)phenoxazone and by immunoassay with defined antiserum specific for P450IIIA. P450IIIA was not detectable (<10 pmol/mg for maternal microsomes and <2 pmol/mg for fetal microsomes) by immunoassay in uninduced maternal or fetal livers. In hepatic microsomes from PCN-induced dams, values ranged from 59.3 to 116 μg P450IIIA1/mg of protein during the same gestational period. Changes in debenzylase activity of 15.9-46.5 pmol of resorufin (mg of protein)$^{-1}$ min^{-1} were consistent with these findings as were the changes in TAO-inhibitable debenzylase activity. In the transplacentally induced fetal liver, debenzylase activity increased steadily from 0.19 pmol of resorufin mg^{-1} min^{-1} at day 15 to 9.34 pmol of resorufin mg^{-1} min^{-1} at day 21 and was paralleled by the TAO-inhibitable activity that ranged from 0.09 pmol of resorufin mg^{-1} min^{-1} at day 15 to 3.33 pmol of resorufin mg^{-1} min^{-1} at day 21. The amount of immunoreactive P450IIIA1 also increased from 0.5 to 28.7 μg/mg of microsomal protein. When the dose of PCN used to induce the maternal animals was increased from 50 mg/kg, once daily for 3 days, to 40 mg/kg, twice daily for 4 days, fetal debenzylase activity was decreased by approximately 10-20% over the gestational period as was the TAO-inhibited debenzylase activity. Analogously, immunoreactive P450IIIA1 was also slightly decreased. The data indicate that P450IIIA1 in fetal rat liver is PCN-inducible as early as day 15 of gestation and that inducibility progressively increases as a function of fetal age.

The cytochromes P450 play a major role in the metabolism of lipophilic exogenous and endogenous substances including drugs, fatty acids, aromatic hydrocarbons, vitamins, pesticides, eicosanoids, and steroids. While P450-dependent metabolism most often serves to detoxify and eliminate active compounds, reactive intermediates may arise. The generation of reactive metabolites and the potential of such metabolites to combine with cellular macromolecules provide an inherent mechanism for profound biologic consequences including carcinogenesis, teratogenesis, and genotoxicity.

This paper focuses on an enzyme of the steroid-inducible subfamily of the P450 cytochromes. Characteristics that distinguish this P450 cytochrome include its inducibility by selective agents and its substrate specificities. P450IIIA1 is

† This work was supported by Grants ES-04041 and ES-03157 from the National Institutes of Health.
* To whom correspondence should be addressed.

0006-2960/89/0428-4871$01.50/0